J Mater Sci: Mater Electron (2023) 34:657

Comparative investigation of magnetic and mechanical properties of nano-Sb_2O_3 and nano-Y_2O_3 addition on bismuth-based superconducting materials

E. B. Cevizci[1,*] and K. Kocabas[2]

[1] *The Graduate School of Natural and Applied Sciences, Dokuz Eylul University, 35390 Izmir, Turkey*
[2] *Department of Physics, Faculty of Science, Dokuz Eylul University, 35390 Izmir, Turkey*

Received: 7 October 2022
Accepted: 2 February 2023
Published online: 1 March 2023

ABSTRACT

Two different nanoparticles with different weight percentages (where x = 0.0, 0.2, 0.4, 0.8, and 1.0 wt%) have been added to the superconducting system with the general formula $Bi_{1,8}Pb_{0,3}Sr_2Ca_2Cu_3O_y + x(A/B)$ (A = Y_2O_3 and B = Sb_2O_3). The samples have been prepared with solid state reaction method. The aim of the study was to investigate and compare the effects of nano-Sb_2O_3 and nano-Y_2O_3 addition on the superconductivity, structural, magnetic, and mechanical properties of the system. X-ray diffraction (XRD), scanning electron microscope (SEM), energy-dispersive spectroscopy (EDX), vibrating sample measurement (VSM), DC resistivity–temperature measurement, and Vickers microhardness measurement (VHM) have been made for samples structural characterizations. XRD analysis presented that samples have orthorhombic crystal structure and both Bi-2223 and Bi-2212 phases coexist in the samples. In SEM photographs, granular structure is plate-like and particles are randomly oriented. M–H measurements have been performed at T = 15 K. Using Bean model, critical current densities have been calculated. Calculated $J(0)$ values are 396 kA/cm^2 and 232 kA/cm^2 for nano-Sb_2O_3 and nano-Y_2O_3, respectively. Nano-Sb_2O_3 additive has been created stronger artificial needling center and higher critical current density than nano-Y_2O_3. R–T results has showed that nano-Sb_2O_3 addition increased critical temperature value (range of 109.92 and 112.48 K), while nano-Y_2O_3 addition decreased (range of 90.53 and 110.68 K). VHM results showed that nano-Y_2O_3 addition samples have bigger hardness values than nano-Sb_2O_3 addition samples. Both doping materials increased the mechanical hardness of the system.

Address correspondence to E-mail: cevizciburcu@gmail.com

https://doi.org/10.1007/s10854-023-10034-4

1 Introduction

$Bi_2Sr_2Ca_{n-1}Cu_nO_{4+2n}$ with formula has three different phases depending on the number of CuO_2 layers (n) in the unit cell [(n = 1, T_C = 20 K) Bi-2201 has single CuO_2 layer; Bi-2212 (n = 2, T_C = 80 K) has double CuO_2 layers, and Bi-2223 (n = 3, T_C = 110 K) have triple CuO_2 layers]. Although Tl and Hg-based high-temperature superconductors with higher critical temperatures are produced, BiSrCaCuO (BSCCO) systems are used widely in a lot of commercial applications. Because it has advantages such as lower toxicity of its constituent powders and including phases with high thermodynamic stability [1, 2]. Also it has large critical current J_c and high upper critical magnetic fields H_{c2}. The presence of secondary phases (Bi-2212, Ca_2PbO_4) in the synthesized Bi-2223 superconductor, intergrain weak links, and other impurity phases adversely affect critical current-carrying capacity under applied high magnetic field. Improvement in the critical current-carrying capacity of BSSCO system is important for applications. Recently, different nano-sized materials have been added to the BSCCO system and their effects on the structural and transport properties of system have been investigated. The dimensions of the nano-sized particles were chosen because they are close to the coherent length, which is related to the size of characteristic Cooper pair [3]. Addition of nanoparticles to these systems can create stronger pinning force in fixing magnetic eddies. Addition of nanoparticles to Bi-2223 has played an important role in flux pinnig and increasing critical current density. This is because nanoparticles are trapped inside the superconductor grains, revealing secondary phase defects and producing crystal defects within the superconducting particles [4].

BSSCO superconducting materials have poor mechanical properties such as less flexibility and high brittleness. These features limit their technological applications. Therefore, one of the important problems is to improve the mechanical properties without disturbing the critical current-carrying capacity and superconductivity parameters [5]. At the same time, nanoparticle addition to various alloys and ceramics has recently attracted great attention due to the effect of increasing mechanical strength of materials and toughening materials [3, 6–9]. With the addition of nano-sized particles, it will be possible to increase both critical current density and mechanical strength of Bi-2223 superconductor system at the same time.

When we examine the studies in literature with micro-scale Sb_2O_3 or Y_2O_3 doping, it draws our attention that Bi-based superconductor system improves superconductivity and mechanical properties in a positive way [10–12]. The presence of Sb plays an effective role in preventing the evaporation of Pb during the calcination process in especially BSSCO system [13]. It was noted that replacement of Sb instead of Pb, Bi, or Sr increased the critical temperature of Bi-2223 systems, from 110 to 132 K (depending on amount of additive) [14–16]. It has also been reported that adding Sb to system not only increases the critical temperature value, but also increases the formation of high-T_C phase (Bi-2223).

In addition, Y_2O_3 nanoparticles were added to Bi-based superconductor systems at different rates. Suazlina et al. [17], reported the effects of Y_2O_3 nanoparticle addition in Bi-2212 superconductors. It was found that critical temperature and critical current density increased up to x = 0.7 wt%. Again, in a study conducted by Oboudi in 2017 [18], nano-Y_2O_3 was added to $Bi_{1,8}Pb_{0,4}Sr_2Ca_2Cu_3O_{10+y}$ superconductor samples with different weight percentages. As the additive ratio increased, the current density increased by 200% and the superconductivity transition temperature increased by 3%. In both studies, it is seen that both the critical temperature and critical current density values of BSCCO system with nano-Y_2O_3 addition increased. In our study, we aimed to investigate the effects of nano-sized Y_2O_3 and nano-sized Sb_2O_3 addition in order to improve the electrical, magnetic, and mechanical properties of BSSCO system. Y_2O_3 nanoparticles were chosen considering the positive effects of BSCCO samples on critical temperature and critical current density values, while Sb_2O_3 nanoparticles were selected considering the improvement of critical temperature values of system by micro-scale Sb_2O_3 additive. The effects of nano-Y_2O_3 particles on magnetic, electrical, and structural properties of BSCCO bulk samples have been studied. Moreover, to the best of our knowledge, there has not been any study about nano-Sb_2O_3 particles effect. The aim of this study is to add both nano-Y_2O_3 and nano-Sb_2O_3 to $Bi_{1.8}Pb_{0.3}Sr_2Ca_2Cu_3O_y$ system at the same rate and under the same preparation conditions and to compare effects of both additives on superconductivity, magnetic, and mechanical properties of this system.

2 Materials and methods

$Bi_{1.8}Pb_{0.3}Sr_2Ca_2Cu_3Oy$ that has nominal composition was synthesized using a solid-state reaction method. Y_2O_3 and Sb_2O_3 nanoparticles were added by small weight percentages (0.2, 0.4, 0.6, 0.8, and 1.0 wt%) in the first step of the synthesis process. $SrCO_3$, CuO, $CaCO_3$, Bi_2O_3, PbO (Aldrich Chem. Co, USA), and nano-sized Sb_2O_3 and nano-sized Y_2O_3 (Nanografi, Turkey) powders with a purity of 99.99% were measured according to their calculated stoichiometric amounts, mixed, and ground. Then mixed powders were calcinated at 820 °C in air for 24 h. The resulting powder was regrounded and then pressed into pellets. Sintering conditions such as temperature and time are very important in producing a good high-T_C superconducting material. For this reason, long sintering times (120 h–150 h) and high sintering temperatures (845 °C–855 °C) are generally preferred when producing BSSCO systems [19]. So the pressed samples were sintered in air at 845 °C for 120 h and cooled down to room temperature. According to their contribution rates (x = 0.0, 0.2, 0.4, 0.8, and 1.0 wt%), nano-Y2O3 addition samples were named as Y0, Y2, Y4, Y8, and Y10 and nano-Sb_2O_3 addition samples were named as Sb0, Sb2, Sb4, Sb8, and Sb10, respectively. Samples prepared by addition nano-Sb_2O_3 and nano-Y_2O_3 were prepared under the same preparation conditions at different time periods.

The lattice parameters, phase purity, crystal structure, and grain size of samples were obtained from X-ray diffraction (XRD, Thermo Scientific ARL X'TRA) with CuK_α radiation at wavelength λ = 0.15406 nm over the range from 3° to 70°. Phase analyses of the samples were determined with the X-powder program. XRD refinements have been made with FullProf Suite ToolBar program (WinPLOTR). The grain structure and surface morphology of the samples were examined with 10000x magnification by scanning electron microscope (SEM, Philips XL 30S) photographs. Energy-dispersive spectrometry (EDS, Philips XL 30S) was applied for the elemental analysis of the samples. Magnetization curves of the samples depending on the magnetic field strength were taken with Vibrating Sample Magnetometer (VSM, LakeShore 747 Vibrating Sample Magnetometer) measurements. Critical current density calculations of samples were made with the data obtained from the M–H curves and Bean Model. Resistance–temperature measurements were made with standard four-probe method between 10 and 300 K (Keithly 6221 DC-AC Current Source and Keithly2182A nanovoltmeter). Microhardness measurements of the samples were made with the Mitutoyo digital microhardness tester of the *HM-200* series.

3 Result and discussion

In Fig. 1a and b, XRD patterns showed that the majority phase consisted of Bi-2223 and Bi-2212 phases in all samples [20]. The presence of $CuSr_2O$ peaks was shown in all nano-Y_2O_3 addition samples. The presence of Ca_2PbO_4 phase at 2θ = 17.8° has been seen in all samples except Y0 and Y2. Secondary phases are an indication that the material could not crystallize completely during heat treatment. Secondary phase defects can occur as a result of modulated displacements of oxygens in the CuO_2 planes in the Bi_2O_2 and CaO layers. The $CaPb_2O_3$ phase plays an important role in accelerating the formation of the Bi-2223 phase [21]. A adequate amount of reactive secondary phases (Bi-2212, $CaPb_2O_4$) formed during the calcination of the powders is necessary for the proper synthesis of Bi-2223 during the sintering step. Secondary phases that cannot participate in the formation of the Bi-2223 phase cause weak intergrain link and weak the flux pinning capacity and the degradation of the orientation of the Bi-2223 platelets [22]. No peaks of Sb_2O_3 and Y_2O_3 nanoparticles were found in the XRD model. The peak intensities of the high-T_C phases have been increased slightly with increasing of nano-Sb_2O_3 addition. As nano-Y_2O_3 addition increased, peak widths have been increased. Except Y0 sample, H115 peak disappeared in all nano-Y_2O_3 addition samples. The peak intensities of low-T_C phase increased slightly with increasing of nano-Y_2O_3 addition.

The volume fraction and the lattice parameters of all samples are listed in Table 1. The volume fraction of Bi-2223 and Bi-2212 phases was calculated according to the equations below using the intensities of the peaks [23]:

$$\text{Bi-[2223]}\ (\%) = \frac{\sum I(2223)}{\sum I(2223) + \sum I(2212)} \times 100 \quad (1)$$

$$\text{Bi-[2212]}\ (\%) = \frac{\sum I(2212)}{\sum I(2223) + \sum I(2212)} \times 100 \quad (2)$$

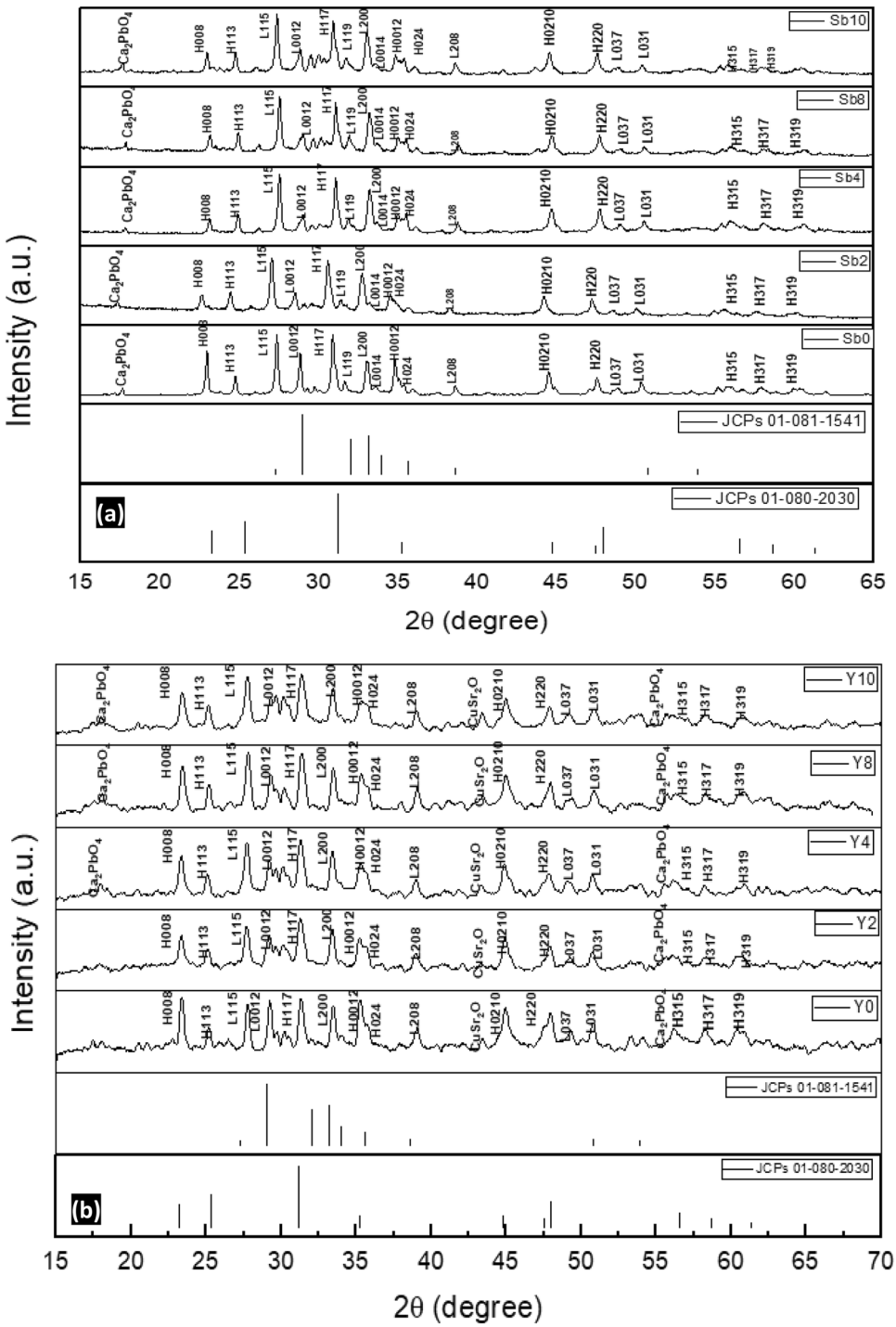

Fig. 1 **a** XRD patterns of $Bi_{1.8}Pb_{0.4}Sr_2Ca_2Cu_3O_{10+\delta} + x(Sb_2O_3)$ system and **b** XRD patterns of $Bi_{1.8}Pb_{0.4}Sr_2Ca_2Cu_3O_y + x(Y_2O_3)$ with (x; wt% 0.0–0.2–0.4–0.8–1.0)

where $I(2223)$ and $I(2212)$ are the intensities of the XRD peaks for Bi-2223 and Bi-2212 phases, respectively. It was observed that the percentage of Bi-2212 phase increased and the percentage of Bi-2223 phase decreased with increasing nano-Y_2O_3. We observed that the decrease in the volume fraction of the Bi-2223 phase in all nano-Sb_2O_3 addition samples was quite small [24]. These results showed that small amounts of nano-Sb_2O_3 addition effectively contribute to the phase stability of BSCCO systems. Both doping materials slightly affected the low -T_c phase (Bi-2212) and high-T_C phase (Bi-2223) ratios [25]. The lattice parameters (a, b, c) are calculated from Miller indices (hkl) and interplanar distances (d_{hkl}) by least squares

Table 1 Calculated lattice parameters (a, b, and c) and volume fraction of pure and nano-additive $Bi_{1,8}Pb_{0,3}Sr_2Ca_2Cu_3O_y + x(A/B)$ ($A = Y_2O_3$ and $B = Sb_2O_3$) samples

Nano-Sb_2O_3	a (Å)	b (Å)	c (Å)	Volume fraction (Bi-2223/Bi-2212)	Nano-Y_2O_3	a (Å)	b (Å)	c (Å)	Volume fraction (Bi-2223/Bi-2212)
Sb0	5.4090	5.3636	37.1964	53.27/46.72	Y0	5.3394	5.3995	37.0740	53.92/46.07
Sb2	5.4036	5.3689	37.1700	54.57/45.42	Y2	5.3488	5.3858	36.9768	50.19/49.80
Sb4	5.4096	5.3608	37.1004	51.85/48.14	Y4	5.3550	5.4081	36.8568	51.55/49.44
Sb8	5.4138	5.3624	37.0308	52.11/47.88	Y8	5.3488	5.3642	36.7716	47.64/52.35
Sb10	5.4096	5.3623	37.0140	52.07/47.92	Y10	5.3412	5.3764	36.7596	48.83/51.16

method for all prepared samples. According to the calculated lattice parameters, crystal lattice of all samples was found to be orthorhombic. The lattice parameters remained almost the same in nano-Sb_2O_3 addition samples. This means that nano-Sb_2O_3 doping did not effect the crystal structure of the system. However, it is thought to play a role as an impurity at the grain boundaries. Similar results were encountered in the study in which our study group previously added nano-SnO_2 to the (Bi)-2223 system [26].

We have seen that while a lattice parameter increased, c lattice parameter decreased in nano-Y_2O_3 addition samples. This behavior can be explained according to two reasons. The first reason may be the replacement of one of the Bi^{3+}, Ca^{2+} or Sr^{2+} ions by Y^{3+} ion. The ionic radius of the Y^{3+} ion (1.02 Å) is smaller than the radius of the Ca^{2+} (1.12 Å), Bi^{3+}(1.17 Å), and Sr^{2+} (1.32 Å) ions in the BSSCO structure. We think that replacement of Y^{3+} of other ions in the structure may cause a decrease in the c parameter. The decrease in c-axis values with increasing nano-Y_2O_3 addition is compatible with Vegard's law [27, 28]. The second reason is thought to be the entry of excess oxygen into the BiO layer. Electrons in the CuO layer, known as the conductivity layer of the BSSCO system, are transferred from the CuO to the BiO layer and lead to the formation of holes in the Cu layers and electrons in the Bi layers according to the following reaction (3) [29]:

$$Bi^{3+} + Cu^{2+} \rightarrow Bi^{3-x} + Cu^{2+x} \quad (3)$$

So the change of c-axis in the nano-Y-added Bi-2223 system is associated with the excess oxygen arising Y_2O_3 molecule. Excess oxygen taken up by the BiO planes results in tighter bonding. Therefore, it decreases the lattice parameter along the c-axis and consequently causes the suppression of superconductivity [30, 31].

Grain size of samples can be estimated using Scherrer formula as shown in Eq. (4) [32].

$$D = \frac{K\lambda}{B\cos(\theta)}, \quad (4)$$

where D is the mean size of grain, B is the line broadening at half the maximum intensity (FWHM) in radians, $\lambda = 0.15406$ nm is the X-ray wavelength, and θ is the Bragg angle. K is Scherrer constant which depends on the crystallite shape and size distribution and indices of the diffraction line [33]. The value of the K constant, which ranges from 0.62 to 2.08, can be affected by microstrain in the crystal. In our study, we assumed $K = 0.9$, which is generally used to calculate the grain size of BSCCO samples with plate-like particle structure, and the calculated D values represent estimates [34, 35]. Grain size of all samples is given in Table 2. The grain size calculation of the samples was calculated by taking average value of the major peaks between 20° and 35°. The grain sizes calculated from XRD patterns lie between 31.63 and 47.23 nm for nano-Sb_2O_3 addition samples. The particle size of the nano-Sb_2O_3 addition samples is smaller than undoped sample. The particle size of nano-Sb_2O_3 addition samples increased with increasing nano-Sb_2O_3 addition. This result was indicated that addition of Sb_2O_3 nanoparticles acts as a bridge and improves the grain growth. It has been seen that nano-Sb_2O_3 makes a positive contribution to improving superconductivity properties of the system by improving intergranular bond. The calculated grain sizes lie between 30.39 and 53.64 nm for nano-Y_2O_3 addition samples. The particle size decreased in Y2 and Y4 samples. After the additive ratio of $X = 0.8\%$, the particle size increased and it was observed that the interparticle bonding began to weaken. It has been seen that nano-Y_2O_3-added

Table 2 Dislocation density, crystallite size, critical current density, and critical temperature values of $Bi_{1,8}Pb_{0,3}Sr_2Ca_2Cu_3O_y + x(A/B)$ ($A = Y_2O_3$ and $B = Sb_2O_3$) samples

Nano-Sb_2O_3	Dislocation density δ (nm^{-2})	Grain size (nm)	$J_c(0)$ (kA/cm^2)	$T_{C,onset}$ (K)	Nano-Y_2O_3	Dislocation density δ (nm^{-2})	Grain size (nm)	$J_c(0)$ (kA/cm^2)	$T_{C,onset}$ (K)
Sb0	0.000448	47.23	293	109.92	Y0	0.000401	49.88	164	109.52
Sb2	0.000999	31.63	309	110.23	Y2	0.001074	30.51	211	110.36
Sb4	0.000860	34.08	299	111.14	Y4	0.001082	30.39	232	110.68
Sb8	0.000733	36.93	289	110.68	Y8	0.000812	35.08	177	98.79
Sb10	0.000589	41.18	396	112.48	Y10	0.000347	53.64	120	90.53

samples began to weaken the intergranular bond of the system above a certain value and make a negative contribution to improving the superconductivity properties of the system. The average particle size of nano-Sb_2O_3-doped samples is smaller than nano-Y_2O_3 addition samples. This may be related to the grinding step of the samples during the preparation process. The Y4 sample has the smallest particle size and the largest dislocation density among nano-Y_2O_3 addition samples. For both doped samples, the particle sizes calculated from the XRD results and the particle development seen from the SEM photographs are similar. The dislocation density (δ) was calculated using the formula $\delta = 1/D^2$ and calculated data are presented in Table 2. It is known that crystalline size and dislocation density vary inversely. As the δ value increases, the crystallinity level decreases [36]. The dislocation density value increased with the increase in the amount of nano-Sb_2O_3. Among all samples, the highest dislocation density belongs to Y2 and Y4 samples. The high hardness value is due to the high dislocation density [37]. These results are confirmed by hardness measurements.

When Figs. 2 and 3 are examined, it is clearly seen that granular structure is plate-like in all samples [38]. It has been seen that particles randomly oriented. The particle size has increased with increasing Y_2O_3 nanoparticles addition. It has been seen that the gaps on the surface of the samples increased and cracks occurred on sample face especially in Y8 and Y10 samples. Bi-2223 phase has weak intergranular links and smaller crystallographic density than Bi-2212 phase. Therefore, in Fig. 2g and i, the sample particle density would be expected to be higher. As can be seen from XRD patterns of the nano-Y_2O_3 addition samples, Y8 and Y10 samples mostly consist of Bi-2212 phase. It has seen that the voids were less in Y2 and Y4 samples. A small addition amount of nano-Y_2O_3 can strengthen the connectivity between grains. The particle size increased with increasing Sb_2O_3 nanoparticles addition. The presence of small point clumps on the surface of nano-Sb_2O_3 addition samples draws attention. As nano-Sb_2O_3 addition increased, the presence of these heaps has been more visible. This result can be considered that nano-Sb_2O_3 particles could not enter the crystal structure, but were trapped in the superconductor grains. Thus, it is considered that the nano-Sb_2O_3 addition appears as secondary phase defect and plays a role in the formation of artificial needling centers on the samples by producing crystal defects in superconducting particles [39]. According to the results of EDX elemental analysis, It is seen that amount of nano-Sb_2O_3 and nano-Y_2O_3 on the samples' surface increases with increasing in addition ratio (%) in both nano-Sb_2O_3 and nano-Y_2O_3 samples. In addition, there is no impurity formation in the material.

Figure 4 shows the resistivity curves as a function of temperature of all samples from 140 K down to 30 K. $T_{C,onset}$ (onset critical temperature) is considered as deviation from the linear behavior of about 110 K. $T_{C,onset}$ values obtained from the resistance–temperature curves are given in Table 2. The critical temperature of nano-Sb_2O_3 addition samples is between 109.92 and 112.48 K. The sample with the highest critical temperature value of 112.48 K is Sb10. Nano-Sb_2O_3 addition increased the critical temperature values of the samples. It is known that micro-scale Sb doping increases the critical temperature value of Bi-based superconducting materials [40]. It has been seen that nano-Sb_2O_3 addition also contributes to the improvement of the critical temperature of the material. The critical temperature of nano-Y_2O_3 addition samples is between 90.53 and 110.68 K.

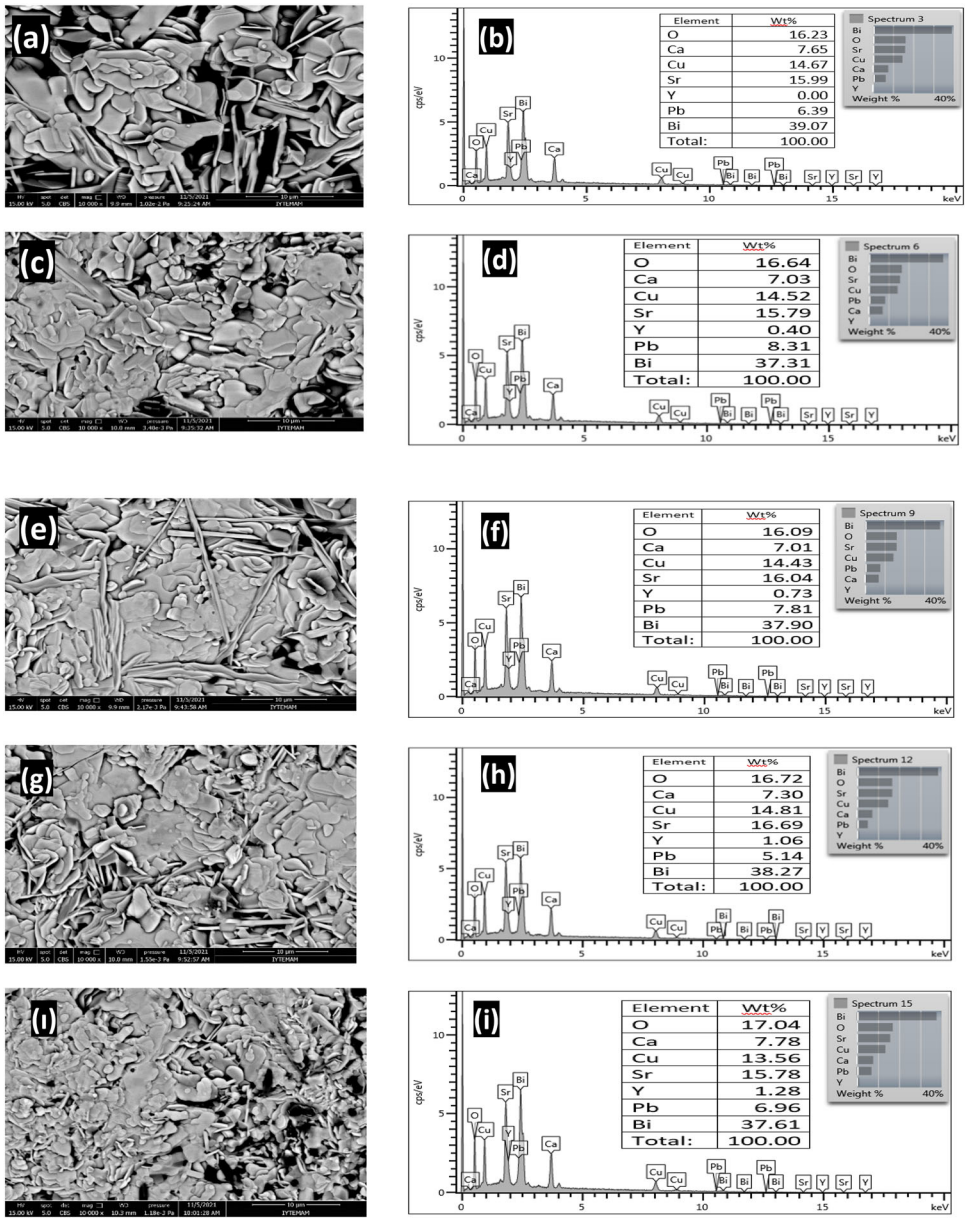

Fig. 2 **a** SEM images of **b** Y0, **c** Y2, **e** Y4, **g** Y8, and **ı** Y10 samples. EDX graphs of **b** Y0, **d** Y2, **f** Y4, **h** Y8, and **i** Y10 samples

The smallest value of the critical temperature belongs to Y10 with 90 K. In nano-Y_2O_3 addition samples, the critical transition temperature of the samples has been not affected significantly up to x = 0.4%. Nano-Y_2O_3 addition decreased the critical temperature values of the samples after x = 0.8% addition. The decrease in critical temperature can be explained by weakening in the bond between intergranular, suppression of superconductivity by nano-Y_2O_3 particles, intergrowth of impurity phases and structural distortions [41]. It is seen from Fıg. 4a and b, two-step phase transitions have been seen in all samples except Y10. The double step is an indication of two phases present in the samples and is related to a structural phase transformation [42]. The samples present two-step features associated with a mixture of Bi-2212 and Bi-2223 phases [43]. Table 3 presents a comparison of the present study's results (T_C and J_C values) and different nanoparticle-added Bi-2223 system's results in the literature. From this table, optimum J_C and T_C values of nano-Sb_2O_3 addition Bi-2223 system are comparable with the good data in the literature.

Magnetic hysteresis loops of the samples are given in Fig. 5a and b. Magnetic measurements were made at field intensity range of H = ± 20,000 Oe at15 K.

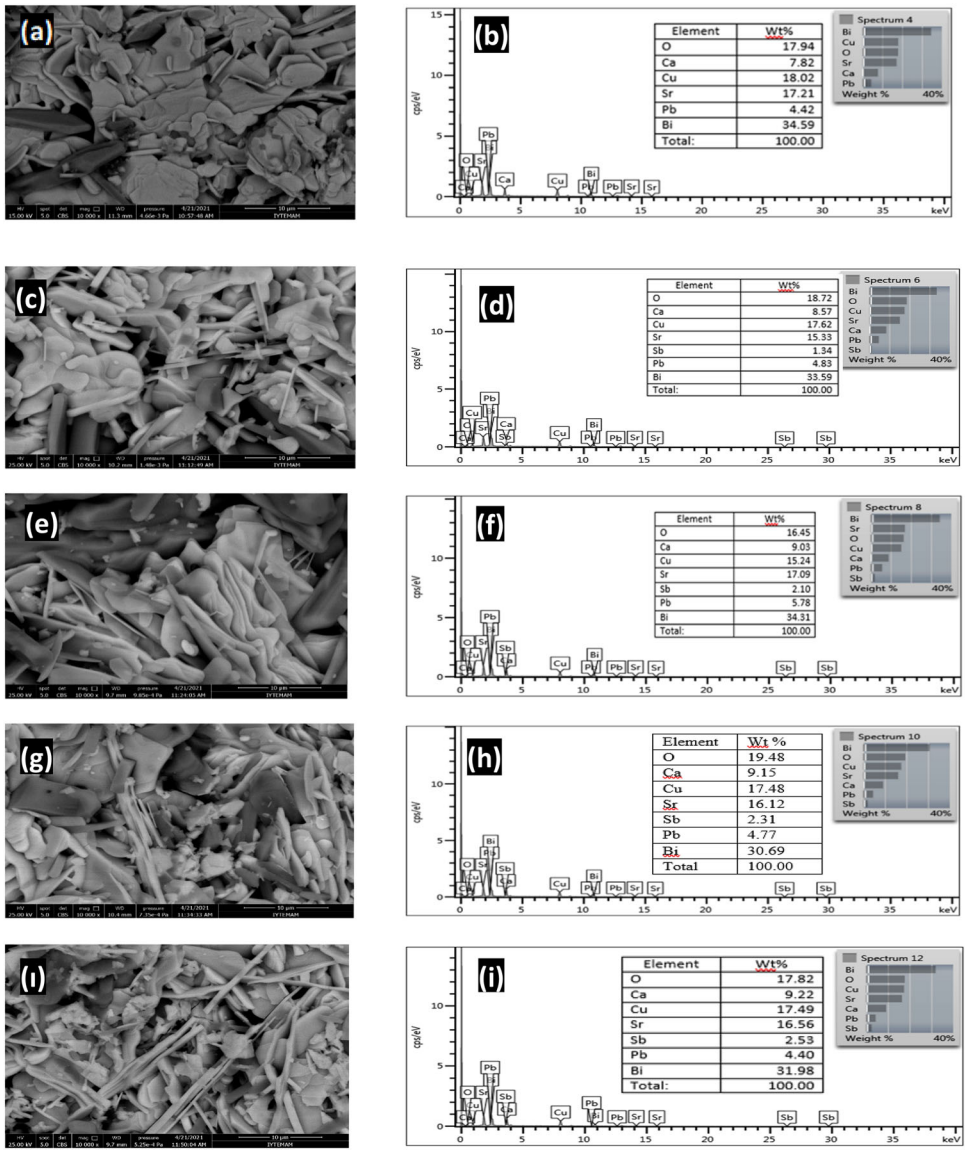

Fig. 3 SEM images of **a** Sb0, **c** Sb2, **e** Sb4, **g** Sb8, and **ı** Sb10 samples. EDX graphs of **b** Sb0, **d** Sb2, **f** Sb4, **h** Sb8, and **i** Sb10 samples

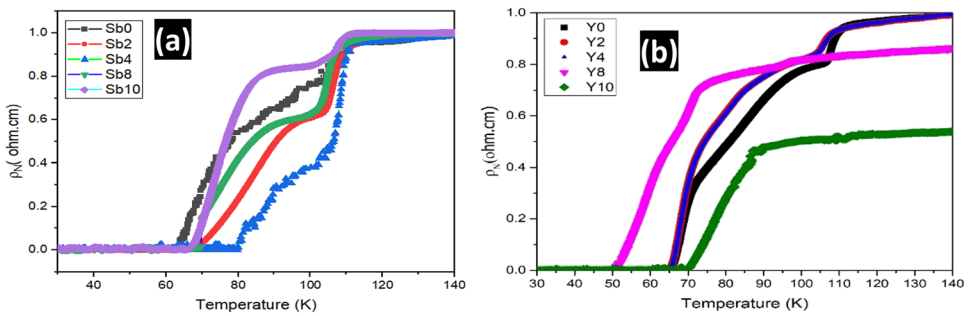

Fig. 4 **a** Resistivity temperature graph of Sb0, Sb2, Sb4, Sb8, and Sb10 samples. **b** Resistivity temperature graph of Y0, Y2, Y4, Y8, and Y10 samples

Magnetic hysteresis loops of superconducting samples give information about magnetic properties of samples and are very useful for analyzing superconductivity properties such as flux needling force and critical current density [44]. When *M*–*H* curves of the samples are examined, it is seen that all samples exhibit a diamagnetic behaviors. The behaviors clearly exhibit the second-type superconductors' features [45]. No break was observed in the curves of the samples. This means that impurity phases in the

Table 3 The comparison of T_c and J_c parameters for nanoaddition Bi-2223 superconductor system

	Additive (type)	Synthesis method	J_c (H = 0) (kA/cm^2)	T_C (K)	References
Bi-2223 + (Sb_2O_3)	NPs	Solid state	3.96×10^5 (15 K)	112.48	Present work
Bi-2223 + (Y_2O_3)	NPs	Solid state	268×10^5 (15 K)	110.68	Present work
Bi-2223 + (Bi_2Te_3)	NPs	Solid state	1×10^{-4} (5 K)	102.00	[25]
Bi-2223 + (Co_3O_4)	NPs	Sol–gel	15.05×10^5 (30 K)	115.30	[41]
Bi-2223 + (MgO)	NPs	Solid state	4.63×10^{-3} (30 K)	109.00	[58]
Bi-2223 + (SiC)	NPs	Sol–gel	16.15×10^5 (10 K)	107.40	[48]
Bi-2223 + (Y_2O_3)	NPs	Solid state	33.85×10^{-3} (77 K)	113.50	[18]
Bi-2223 + (Y_2O_3)	NPs	Solid state	4.87×10^{-3} (30 K)	69.00	[17]
Bi-2223 + (Eu_2O_3)	NPs	Sol–gel	10.33×10^{-3} (77 K)	107.00	[8]

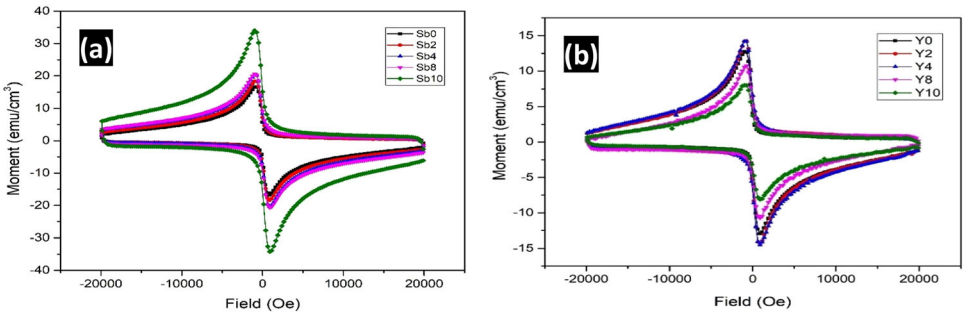

Fig. 5 **a** M–H hysteresis loop of Sb0, Sb2, Sb4, Sb8 and Sb10 samples at 15 K. **b** M–H hysteresis loop of Y0, Y2, Y4, Y8, and Y10 samples at 15 K

samples are not evident. The result obtained from M–H curves is in agreement with the results of XRD measurements. Formation of undesirable phases, the quality of the microstructure, and the length of coherence affect the magnetic hysteresis loop size [2].

Fig. 5a and b shows the M–H hysteresis loops of nano-Sb_2O_3 and nano-Y_2O_3 addition samples, respectively. It has been seen that the surface area of the samples with Sb_2O_3 nanoparticle addition is larger than the surface area of the samples with Y_2O_3 addition. One of reasons is that nano-Sb_2O_3 particles can create a stronger needling center than nano-Y_2O_3 particles. The other reason is that samples' sizes were different which were used in M–H measurement. The surface of magnetization curves is tightly dependent on the sample sizes. The surface areas of hysteresis loops increases with increasing nano-Sb_2O_3 addition up to x = 1.0%. S10 sample showed the widest hysteresis loop. Nano-Sb_2O_3 addition increased the magnitude of magnetization curves by creating artificial pinning centers. In Fig. 5b, the surface area of hysteresis loops of the Y2 sample is the largest. The decrease in the hysteresis loops with increasing nano-Y_2O_3 addition indicates that non-superconducting regions increased in size [46].

The magnetic field dependence of J_c was calculated by using the experimental Bean model shown in Eq. (5).

$$j_c = 20 \times \frac{\Delta M}{a\left(1 - \frac{a}{3b}\right)} \tag{5}$$

M is the value in the equation. It is the magnetization value obtained from the M–H curves. $\Delta M[\Delta M = (M^+) - (M^-)]$ is the width of the magnetization curve during the decrease and increase of the area in emu/cm^3. M^+ and M^- are the values of positive and negative region band of the magnetic response of samples against the external magnetic field , respectively. The values of a and b ($a < b$) are the dimensions of the rectangular cross section of the sample perpendicular to the applied area in cm [47].

Figure 6a and b shows the J_c at 15 K of nano-Sb_2O_3 addition and nano-Y_2O_3 addition samples, respectively. It has been seen in the graphs that J_c values of the samples decreased as the magnetic field increased [48]. It is thought that reason for the decrease in the diamagnetic properties of the samples is due to weakening of interparticle bond [49]. According to the calculations, the J_C value of the doped samples is higher than the critical current density of the

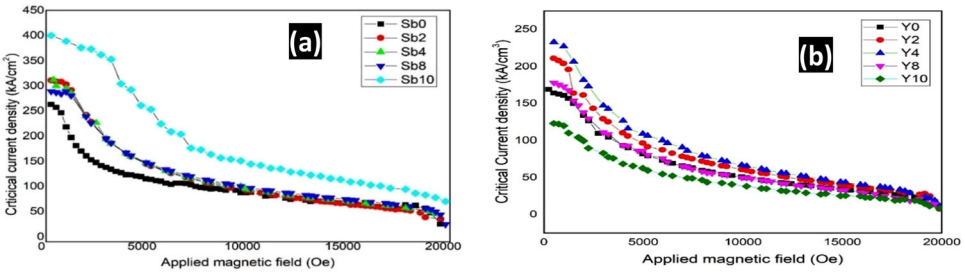

Fig. 6 Field dependence of critical current density at 15 K for **a** Sb0, Sb2, Sb4, Sb8 and Sb10 samples, **b** 15 K for Y0, Y2, Y4, Y8, and Y10 samples

undoped samples. In Table 2, the highest $J_c(0)$ value for sample Sb10 is 396 kA/cm^2. J_c critical current density increases with increasing nano-Sb_2O_3 addition samples, as it supports the *M*–*H* curves. The nano-Sb_2O_3 particles could act as artificial needling centers. Nano-Sb_2O_3 particles can act role as flux fixation centers within the Bi-2223 lattice. And they can increase effectively the critical current density [50]. In Table 2, the highest $J_c(0)$ value for sample Y4 is 232 kA/cm^2. Except for the Y10 sample, the critical current density value of all samples is higher than undoped sample. Nano-Y_2O_3 addition has a positive contribution to the formation of artificial needling centers as it is in nano-Sb_2O_3 addition [51]. We clearly see that critical current density values of nano-Sb_2O_3 addition samples are higher than Y_2O_3-doped samples. The change in the critical current density depends on the formation of trapping centers in the structure and intergranular bond. However, since all of the samples were prepared under the same conditions, considering that the intergranular coupling would be similar in the samples. This irregular change in the critical current density values can only be explained by the increase and decrease in the trapping centers.

The microhardness values were measured for five different (0.294, 0.490, 0.980, 1.961, and 2.940 N) loads values on samples' surfaces. Measurements were taken using the Vickers pyramidal indenter, and the loading time of the force is 10 s. Indentations were pressed on different parts of the samples' surfaces. Microhardness values were determined by taking average value of all measurements.

$$H_v = 1854.4\left(\frac{F}{d^2}\right)\ (\mathrm{GPa}) \tag{6}$$

Vickers microhardness was calculated using Eq. (6) given above [52, 53]. The applied load is *F* (N) and *d* is the average diagonal length of the indentation impression (μm).

In Fig. 7a and b, it has been observed that microhardness value of samples increased with increasing applied load, and these behavior is known as reverse indentation size effect (RISE) in the literature. RISE behavior is a result of bond strength between superconducting grains and is caused by indentation-induced cracking. These materials show only plastic deformation [54]. In Meyer's law given by the equation $F = Ad^{nk}$, A is a load-independent constant and n_k is the Meyer number, which is a measure of ISE or RISE behavior. In *F*–In*d*, graphs of all samples and slope of each graphs are given in Fig. 8a and b. The n_k values of all samples are greater than 1.6. (According to Meyer Law: İf the value n_k is $1 < n_k < 1.6$, material is hard; if the value n_k is $n_k > 1.6$, material is soft) [55]. The produced samples are soft material.Y4 sample has the highest hardness value. As supported by XRD results, compared to other nano-Y_2O_3-addition samples, the dislocation density of the Y4 sample is larger and the particle size is smaller. As the particle size gets smaller, the bond between the superconducting particles gets stronger and the mechanical strength is expected to increase. The hardness value of the doped samples is decreased after $x = 0.4\%$ additive value. We think that the decrease in microhardness with increasing additive content may be due to the weakening of the bond between superconducting grains and randomly distributed irregularities at grain boundaries [56]. In the surface, micrographs of samples showed that grain sizes, porosity, and surface cracks increase as nano-Y_2O_3-addition increases (Fig. 2i). When the microhardness of the nano-Sb_2O_3 addition samples is examined, it is seen that the hardness values of the doped samples increase compared to the undoped samples. The hardness value of the sample with $x = 0.1\%$ added, called Sb 10, is the highest. It has seen that the nano-Sb_2O_3 addition increases the mechanical strength by positively affecting the hardness value of the structure. The increased hardness with the addition of nano-

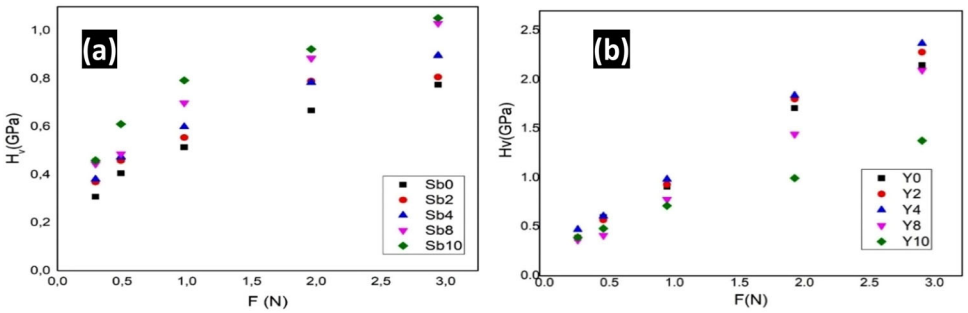

Fig. 7 **a** Variation of load-dependent microhardness H_v of nano-Sb doped samples with applied load F. **b** Variation of load-dependent microhardness H_v of nano-Y doped samples with applied load F.

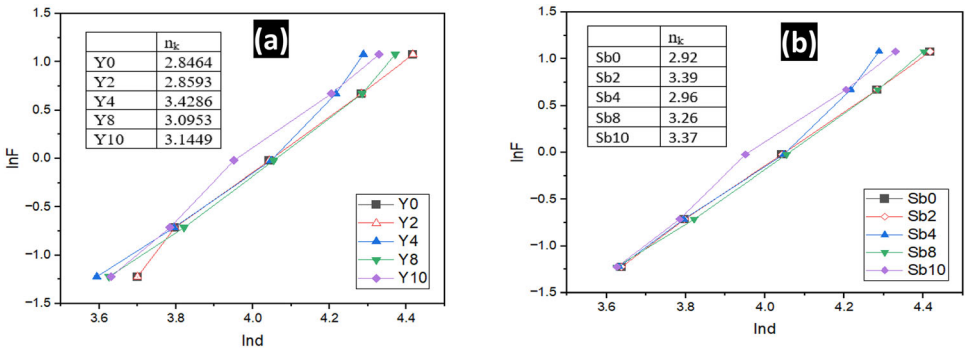

Fig. 8 ln$F$–ln$d$ graphs of **a** Y0, Y2, Y4, Y8, and Y10 samples, **b** Sb0, Sb2, Sb4, Sb8, and Sb10 samples

Sb_2O_3 to the BSSCO system can be caused by both the fixation of dislocations in the impurity regions and defects in the crystal due to impurity atoms. At the same time, the increase in the H_v hardness value can be attributed to the decrease in porosity, the strengthening of the intergranular bond, and the increase in resistance to crack propagation [57].

The hardness values of the undoped samples were measured very close to each other in both doped samples. When the hardness values of the samples with nano-Sb_2O_3 and nano-Y_2O_3 are compared with each other, the hardness values of the samples with nano-Y_2O_3 addition are higher than the hardness values of the samples with nano-Sb_2O_3 addition. Both nano-Sb_2O_3 and nano-Y_2O_3 doping increased the hardness values of Bi-based superconductor samples, which was prepared under the same conditions. It is seen that both additives made to the BSSCO system increase the mechanical strength by positively affecting the hardness value of the structure.

4 Conclusion

Based on the results of measurements, the following conclusions can be summarized as:

- To the XRD results, all the samples consisted of Bi-2212 phases, Bi-2223 phases, and Ca_2PbO_4 impurity phases. No peaks belong to Sb_2O_3 and Y_2O_3 nanoparticles were found in the XRD patterns.
- While a lattice parameter increased, c lattice parameter decreased in nano-Y_2O_3 addition samples. The lattice parameters remained almost the same in nano-Sb_2O_3 addition samples.
- To the SEM photographs, it has been seen that the particle structure was plate-like. The grain sizes of both systems ranged from 30.39 to 53.64 nm. The particle size of doped samples increased with increasing both nan-Y_2O_3 and nano-Sb_2O_3 addition.
- EDX analysis confirmed that there are no impurity elements present in the materials. It has been seen that all elements are included in the structure.
- The critical temperature values of nano-Sb_2O_3 addition samples are between 109.92 and 112.48 K. The critical temperature values of nano-Y_2O_3 addition samples are between 90.53 and 110.68 K. The critical temperature values of nano-Sb_2O_3 addition samples increased more than nano-Y_2O_3 addition samples.
- When the M–H curves of the samples are examined, all samples showed diamagnetic properties. The critical current density values of nano-Sb_2O_3

addition samples are higher than nano-Y_2O_3 addition samples.

- The hardness values of nano-Y_2O_3 addition samples are higher than nano-Sb_2O_3 addition samples. Both nano-sized additives increased the mechanical hardness of the system. It has been seen that all samples are soft material according to Meyer's Law.

Acknowledgments

We would like to thank Dokuz Eylül University faculty member Dr. Özlem Bilgili and İzmir University of Economics Faculty Member Hasan Durmuş for their valuable advice.

Author contributions

All authors contributed to the formation of the idea phase of the study and to the design of the study. EBC takes part in the preparation, data collection, and analysis of the material. KK created the first draft of the manuscript. All authors have commented on previous versions of the article. The manuscript was read and approved by all authors.

Funding

The authors declared that they did not receive any financial support, funds, or grants during this study.

Data availability

Scanning electron microscopy images and raw data of X-ray diffraction patterns were taken at Izmir Institute of Technology – Center for Material Research. Raw data of magnetization measurements were taken at Central Research Laboratory of Kastamonu University. Data derived by the authors are available from the corresponding authors upon request.

Declarations

Conflict of interest The authors have no financial or non-financial interests to disclose.

References

1. C. Michel, M. Hervieu, M.M. Borel, A. Grandin, F. Deslandes, J. Provost, B. Raveau, Z. Phys. B Condens. Mater. **68**, 421 (1987)
2. U. Oztornacı, B. Ozkurt, Ceram. Int. **43**, 5 (2017)
3. M. Roumié, S. Marhaba, R. Awad, M. Kork, I. Hassan, R. Mawassi, J. Supercond. Nov. Magn. **27**, 1 (2014)
4. A. Abou-Aly, M.M.H. Abdel Gawad, R. Awad, I. G-Eldeen, J. Supercond. Nov. Magn. **24**, 7 (2011)
5. B. Cevizci, O. Bilgili, K. Kocabas, J. Mater. Sci. Mater. Electron. **27**, 12 (2016)
6. R. Awad, A. Abou-Aly, M.M.H. Abdel Gawad, I. G-Eldeen, J. Supercond. Nov. Magn. **25**, 4 (2012)
7. M. Hafiz, R. Abd-Shukor, Adv. Mater. Res. **895**, 10226680 (2014)
8. A. Zelati, A. Amirabadizadeh, A. Kompany, H. Salamati, J. Sonier, J. Supercond. Nov. Magn. **27**, 6 (2014)
9. T. Çorduk, O. Bilgili, K. Kemal, J. Mater. Sci. Mater. Electron. **28**, 11 (2017)
10. S. Altin, M.A. Aksan, M.E. Yakinci, Solid State Sci. **13**, 5 (2011)
11. M. Romero-Sanchez, T. Sanchez-Mera, J. Santos-Cruz, C.E. Pérez-García, M.L. Olvera, C.R. Santillán-Rodríguez, J. Matutes Aquino, G. Contreras-Puente, F. Moure-Flores, Ceram. Int. **48**, 11 (2022)
12. Y. Dong, A. Sun, B. Xu, H. Zhang, M. Zhang, Mod. Phys. Lett. B **30**, 26 (2016)
13. V. Fruth, M. Popa, A. Ianculescu, M. Stir, S. Preda, G. Aldica, J. Eur. Ceram. Soc. **24**, 6 (2004)
14. H. Azhan, K. Azman, S.Y.S. Yusainee, Solid State Sci. Technol. **17**, 1 (2009)
15. L. Hongbao, E. Xiaonong, C. Yaozu, R. Yaozhong, C. Zhaojiia, E. Yuheng, Physica C **156**, 804 (1988)
16. E.K. Cam, K. Kocabas, J. Mater. Sci. Mater. Electron. **27**, 8 (2016)
17. M.A. Suazlina, S.Y.S. Yusainee, H. Azhan, R. Abd-Shukor, R. Mustaqim, J. Teknol. Sci. Eng. **69**, 2 (2014). https://doi.org/10.11113/jt.v69.3106
18. S.F. Oboudi, J. Supercond. Nov. Magn. (2017). https://doi.org/10.1007/s10948-016-3939-7
19. N.D. Zhigadlo, V.V. Petrashko, Y.A. Semenenko, C. Panagopoulos, J.R. Cooper, E.K.H. Salje, Physica C **299**, 327 (1998)
20. L.A. Mohammed, K.A. Jasim, J. Phys. Conf. Ser. **1879**, 032069 (2021)
21. T.T. Dung, P.T. An, T.B. Duong, N.K. Man, N.T.M. Hien, T.H. Duc, J. Sci. Mater. Phys. **37**, 4 (2021)
22. V. Garnier, A. Ambrosini, G. Desgardin, J. Mater. Sci. Mater. Electron. **37**, 9 (2002)

23. G. Yildirim, A. Varilci, M. Akdogan, C. Terzioglu, J. Mater. Sci. Mater. Electron. **23**, 8 (2012)
24. A. Agail, R. Abd-Shukor, Solid State Sci. Technol. **22**, 1–2 (2014)
25. M.S. Shalaby, M.H. Hamed, N.M. Yousif, H.M. Hashem, Ceram. Int. **47**, 18 (2021)
26. S. Yavuz, O. Bilgili, K. Kemal, J. Mater. Sci. Mater. Electron. **27**, 5 (2016)
27. N. Ahmad, S. Khan, M.M.N. Ansari, Ceram. Int. **44**, 13 (2018)
28. L. Vegard, Eur. Phys. J. A **5**, 1 (1921)
29. A. Sedky, Physica C **468**, 14 (2008)
30. A. Sedky, J. Phys. Chem. Solids **70**, 2 (2009)
31. M.F.N. Boussouf, A. Mosbah, A. Amira, S.P. Varilci, M. Altintas, M. Guerioune, J. Supercond. Nov. Magn. **26**, 155719390 (2013)
32. P. Scherrer, Nachr. Ges Wiss Göttingen **26**, 98 (1918)
33. J.I. Langford, A.J.C. Wilson, J. Appl. Crystallogr. **11**, 102 (1978)
34. M.E. Kır, B. Özkurt, M.E. Aytekin, Physica B **490**, 79–85 (2016)
35. O. Bilgili, K. Kocabas, J. Mater. Sci. Mater. Electron. **25**, 2889–2897 (2014)
36. O. Bilgili, J. Low Temp. Phys. **204**, 5–6 (2021)
37. W. Li, M. Vittorietti, G. Jongbloedb, J. Sietsma, J. Mater. Sci. Technol. **45**, 35–43 (2020)
38. S. Safran, H. Ozturk, F. Bulut, O. Ozturk, Ceram. İnt. **43**, 17 (2017)
39. H. Fallah-Arani, S. Baghshahi, A. Sedghi, D. Stornaiuolo, F. Tafuri, D. Massarotti, N. Riahi-Noori, Ceram. İnt. **44**, 5209–5218 (2018)
40. K. Kocabas, M. Ciftcioglu, Phys. Status Solidi **177**, 2 (2000)
41. A.N. Jannah, H. Abdullah, IOP Conf. Ser. Mater. Sci. Eng. **395**, 012007 (2018)
42. C. Terzioglu, M. Yilmazlar, O. Ozturk, E. Yanmaz, Physica C **423**, 119 (2005)
43. N. Türk, H. Gündoğmus, M. Akyol, D. Yakıncı, A. Ekicibil, B. Ozçelik, J. Supercond. Nov. Magn. **27**, 3 (2014)
44. M. Romero-S´anchez, T. Sanchez-Mera, J. Santos-Cruz, C.E. P´erez-García, M. de la L. Olvera, C.R. Santillan-Rodríguez, J. Matutes-Aquino, G. Contreras-Puente, F. de Moure-Flores, Ceram. Int. **48**, 11 (2022)
45. B. Ozkurt, J. Mater. Sci. Technol. **24**, 11 (2013)
46. H. Gundogmus, J. Mater. Sci. Mater. Electron. **28**, 6 (2017)
47. C.P. Bean, Phys. Rev. Lett. **8**, 250 (1962)
48. H. Fallah-Arani, H. Koohani, F.S. Tehrani, N.R. Noori, N.J. Nodoushan, Ceram. İnt. **48**, 21 (2022)
49. N.A.A. Yahya, R. Abd-Shukor, J. Supercond Nov. Magn. **27**, 329–335 (2014)
50. A. Ghattas, M. Annabi, M. Zouaoui, F. Ben Azzouz, M. Ben Salem, Phys. C **468**, 1 (2008)
51. Z.Y. Jia, H. Tang, Z.Q. Yang, Y.T. Xing, Y.Z. Wang, G.W. Qiao, Phys. C Supercond. **337**, 1–4 (2000)
52. S.M. Khalil, A. Sedky, Physica B **357**, 299–304 (2005)
53. O. Ozturk, E. Asikuzun, A.T. Tasci, T. Gokcen, H. Ada, H. Koralay, S. Cavdar, J. Mater. Sci. Mater. Electron. **29**, 3957–3966 (2018)
54. H. Ozturk, S. Safran, J. Alloys Compd. **731**, 831–838 (2018)
55. K. Sangwal, Mater. Chem. Phys. **63**, 2 (2000)
56. B. Ozkurt, J. Supercond. Nov. Magn. **26**, 2 (2013)
57. U. Kolemen, O. Uzun, C. Emeksiz, F. Yılmaz, A. Coskun, A. Ekicibil, B. Ozcelik, J. Supercond. Nov. Magn. **26**, 11 (2013)
58. N.A.A. Yahya, R. Abd-Shukor, J. Supercond. Nov. Magn. **27**, 329–335 (2014)